Demonstrating robust simulation of driven-dissipative problems on near-term quantum computers

Brian Rost,^{1,4*} Lorenzo Del Re,¹ Nathan Earnest,² Alexander F. Kemper,³ Barbara Jones,⁴ James K. Freericks¹

¹Department of Physics, Georgetown University; Washington DC.
 ²IBM Quantum, IBM T.J. Watson Research Center; Yorktown Heights, New York.
 ³Department of Physics, North Carolina State University; Raleigh, North Carolina.
 ⁴IBM Quantum, IBM Research Almaden; San Jose, California.

*E-mail: bwr5@georgetown.edu

Quantum computers are poised to revolutionize the simulation of quantum-mechanical systems in physics and chemistry. Current quantum computers execute their algorithms imperfectly, due to uncorrected noise, gate errors, and decoherence. This severely limits the size and scope of protocols which can be run on near-term quantum hardware. Much research has been focused on building more robust hardware to address this issue, however the advantages of more robust algorithms remains largely unexplored. Here we show that algorithms for solving the driven-dissipative many-body problem, among the hardest problems in quantum mechanics, are inherently robust against errors. We find it is possible to solve dissipative problems requiring deep circuits on current quantum devices due to the contractive nature of their time evolution maps. We simulate one thousand steps of time evolution for the non-interacting limit of the infinite driven-dissipative Hubbard model, calculate the current through the system and prepare a thermal state of the atomic limit of the Hubbard model. These problems were solved using circuits containing up to two thousand entangling gates on quantum computers made available by IBM, showing no signs of decreasing fidelity at long times. Our results demonstrate that algorithms for simulating dissipative problems are able to far out-perform similarly complex non-dissipative algorithms on noisy hardware. Our two algorithmic primitives are the basic building blocks of many condensedmatter-physics systems, and we anticipate their demonstrated robustness to hold when generalized to solve the full many-body driven-dissipative quantum problem. Building upon the algorithms presented here may prove to be the most promising approach to tackle important, classically intractable problems on quantum computers before error correction is available.

Introduction

One of the grand challenges in science is to understand the behavior of driven-dissipative quantum systems. While the general formalism for the nonequilibrium problem was introduced in the 1960s, it is only recently that conventional computers have begun to be able to solve some of these problems; a general long-time nonequilibrium many-body quantum solver does not exist for conventional computers. In this work, we show that quantum computers with reset gates, even noisy intermediate-scale quantum (NISQ) computers, have the potential to solve these problems in the near future.

The nonequilibrium many-body problem is a frontier of research in many different disciplines: (i) in condensed-matter physics, pump-probe experiments drive a system into nonequilibrium and watch how it evolves [1]; (ii) in chemistry, driving and dissipation play important roles in photochemistry [2] and in cavity-enhanced reactions [3]; (iii) in nuclear and high-energy physics, collisions of heavy nuclei induce nonequilibrium dynamics [4]; and many more. A prototypical example found in condensed matter physics is a pump-probe experiment. In such an experiment, an ultrashort high-energy pump pulse excites the crystal to a high-energy state that is far from

equilibrium, and the system is then probed with different time delays afterwards to determine what state was created, and how that state relaxes. In some cases, the system is driven to new (meta)stable nonequilibrium phases that cannot be produced any other way. Within the many-body problem, the two simplest types of dissipative dynamics are (i) dynamics that dissipate to a steady thermal state and (ii) driven dynamics in response to a constant external field. We discuss both cases in this work.

Although many quantum algorithms are known for the simulation of closed quantum systems, fewer studies have considered the simulation of open quantum systems despite their rich and interesting behavior[5]. Current approaches include using inherent qubit decoherence[6, 7, 8], direct simulation of an environment[9, 10, 11], implementing Kraus maps / Lindblad operators[12, 13, 14, 15, 16], variational techniques[17, 18], and more [19, 20]. Since Barreiro et al. first demonstrated their open-system quantum simulator[21], current early-stage dissipative simulations of quantum systems in the areas of quantum chemistry and physics [19, 12, 7, 22] have been completed.

While fault-tolerant quantum computers will be robust for many types of algorithms[23], current hardware has too many errors to be able to carry out long-time coherent quantum evolution[24]. The time evolution for driven-dissipative systems is intrinsically error mitigating[25, 26, 27] and it can be carried out to much longer times than coherent time evolution. With the advent of reset gates being available on quantum computers, this opens up a new realm of computation, where NISQ devices can be focused on solving this important and difficult quantum problem.

Kraus Maps

The time evolution of a system driven out of equilibrium by an external field that dissipates energy (through the coupling with a reservoir) is not unitary; it is described by a completely positive trace preserving map (also known as a Kraus map)[5]. The density matrix of the system at time $t+\Delta t$, $\rho(t+\Delta t)$, can be constructed from $\rho(t)$ via a (time-dependent) Kraus map in the following way:

$$\rho(t+\Delta t) = \sum_{i} K_{i}(t) \, \rho(t) \, K_{i}^{\dagger}(t), \tag{1}$$

where the Kraus operators $K_i(t)$ satisfy the sum rule $\sum_i K_i^{\dagger}(t) K_i(t) = \mathbb{I}$. Since Kraus maps are nonunitary, they are difficult to directly apply on quantum computers via universal (reversible) gates. Instead, we implement dissipative dynamics via irreversible processes using selective resets during the computation. When driving toward a time-periodic

"steady" state, the target goal at each time step changes with time, but because the Trotterized Kraus map at each time step maps all inputs towards a single output, errors in one step tend to be mitigated in subsequent steps. This makes the time evolution for dissipative dynamics inherently robust to errors and well suited for NISQ devices, as discussed further in the supplemental information.

Because of this inherent stability and because these problems are challenging to solve on conventional computers, the driven-dissipative problem may be the best application for near-term quantum computing. In this work, we illustrate how dissipative quantum simulation can be performed on IBM's quantum computers by considering two problems: the driven-dissipative Hubbard model in its non-interacting and atomic limits.

Non-Interacting Limit

First, we examine the non-interacting limit of the drivendissipative Hubbard model, whose full details are given in Suppl. 2. This model consists of electrons freely moving on an infinite one-dimensional lattice having semi-infinite electronic thermal reservoirs (taken in the wide-band limit) attached to each lattice site. The Hamiltonian of the thermal reservoirs is given by

$$\hat{\mathcal{H}}_b = \sum_{i\alpha} \omega_\alpha c_{i\alpha}^\dagger c_{i\alpha} \tag{2}$$

where α runs over the infinite internal degrees of freedom of the reservoir and i indexes the lattice sites and $c_{i\alpha}$ annihilates a reservoir electron with indices i and α .

The lattice electrons move via nearest-neighbor hopping with amplitude γ_h (used as our energy unit). A DC electric field of strength E is applied by employing a linearly varying Peierls phase in the lattice hopping and summarized by $\Omega=eEa$, with e the electric charge and a the lattice spacing (we set \hbar and c to one). Our system Hamiltonian then reads

$$\hat{\mathcal{H}} = -\gamma_h \sum_{i} \left[e^{i\Omega t} d_i^{\dagger} d_{i+1} + e^{-i\Omega t} d_{i+1}^{\dagger} d_i \right]$$
 (3)

where d_i annihilates a lattice electron at site i.

Each reservoir is coupled via a lattice-reservoir hopping term to the system at each lattice site

$$\hat{\mathcal{V}} = -g \sum_{i\alpha} \left(d_i^{\dagger} c_{i\alpha} + c_{i\alpha}^{\dagger} d_i \right). \tag{4}$$

where g is the bare hybridization amplitude. We'll find it convenient to describe this coupling in terms of the parameter $\Gamma=g^2N(0)$ with N(0) being the reservoir DOS evaluated at the Fermi level.

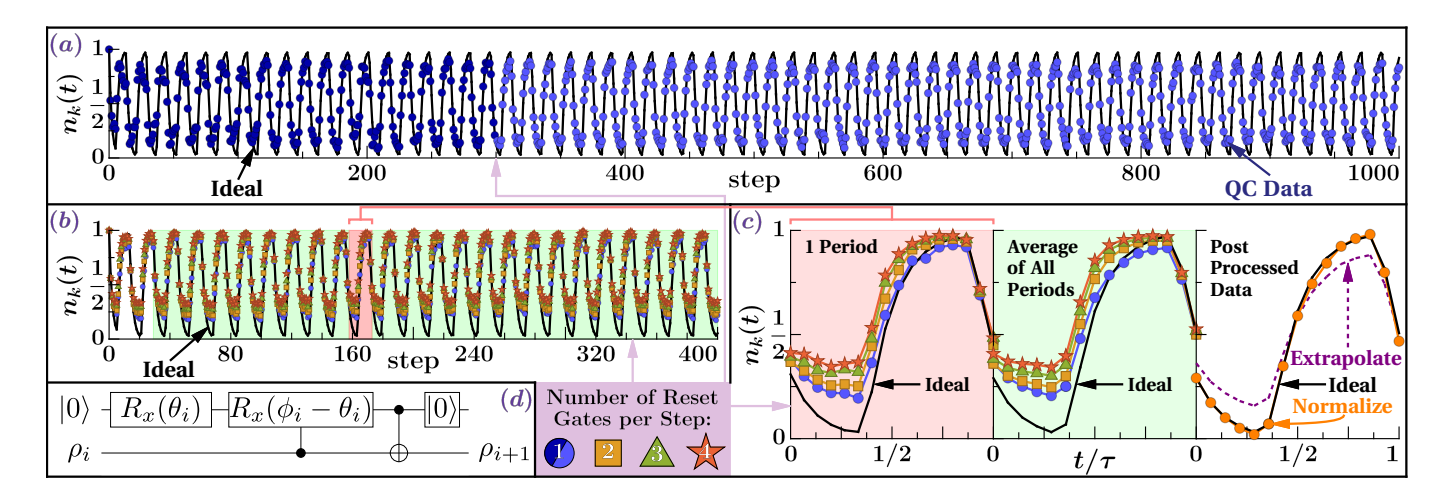


Figure 1: Electron density vs. time. (a) 1000 steps of time evolution on ibmq_mumbai using one reset gate per Trotter step. Reported data has been corrected for measurement errors. Different shades of blue represent different sets of qubits while the solid black line is the ideal result of running the circuit. (b) 400 steps of time evolution on ibmq_boeblingen using one to four reset gates per Trotter step. Reported data has been corrected for measurement errors. (c) Left panel shows a zoom in on one period of the data shown in (b). Middle panel shows one period of data obtained by averaging together all periods of steady-state data (step > 30). Right panel shows post-processed averaged data as described in supplement 5. (d) Quantum circuit for one Trotter step of time evolution. Here, $\theta_i = 2\sin^{-1}\sqrt{\frac{2\Gamma\Delta t}{e^{\beta\varepsilon_i+1}}}$ and $\phi_i = 2\sin^{-1}\sqrt{\frac{2\Gamma\Delta t}{e^{-\beta\varepsilon_i+1}}}$ where $\varepsilon_i = -2\cos(k + \Omega i \Delta t)$ is the dispersion relation at step i (at time $t = i\Delta t$).

The infinite system is diagonalized by Fourier transforming to momentum space. In this fashion, the dynamics of the infinite lattice is addressed by solving many independent one-qubit systems, each of which depends on the specific value of the crystalline momentum k; in the steady state, we construct the results for all momenta from the results for any single momentum by invoking gauge invariance, as described in Suppl. 2.

The time and momentum dependent Kraus operators (for the time step of duration Δt) are given by:

$$K_{0} = d_{k}^{\dagger} d_{k} \sqrt{1 - 2 \Gamma n_{F} [-\epsilon_{k}(t)] \Delta t} e^{-i\epsilon_{k}(t) \Delta t}$$

$$+ d_{k} d_{k}^{\dagger} \sqrt{1 - 2 \Gamma n_{F} [\epsilon_{k}(t)] \Delta t}$$

$$K_{1} = \sqrt{2 \Gamma \Delta t} n_{F} [\epsilon_{k}(t)] d_{k}^{\dagger}$$

$$K_{2} = \sqrt{2 \Gamma \Delta t} n_{F} [-\epsilon_{k}(t)] d_{k},$$

$$(5)$$

where d_k^{\dagger} is the creation operator of a lattice electron with momentum k, $\epsilon_k(t)$ is the time dependent dispersion relation, and $n_F(x)=1/(1+e^{\beta x})$ is the Fermi-Dirac distribution at the temperature of the reservoirs (here set to $\beta=\frac{1}{k_BT}=5$). From the Kraus map given in Eq. 5 the quantum circuit can

From the Kraus map given in Eq. 5 the quantum circuit can be constructed [28] and appears in Fig. 1(d). The $|0\rangle$ gate in the circuit is a reset operation which ideally sets the qubit to the $|0\rangle$ state. However, this operation is not perfect on current

hardware and the reset fidelity can be improved by applying it to a qubit multiple times in succession (at the cost of additional amplitude damping on the remaining qubits). We run our circuit using one to four reset gates per Trotter step to extrapolate away some of these errors. Details are given in supplement 4.

Figure 1(a) plots the results of running the circuit shown in 1(d) with a single reset gate per Trotter step. The first 300 steps were run on one set of qubits and the remaining 700 on a second set. These runs are robust both with respect to the qubits run on and with respect to the total time of the run. The circuit for the 1000th step required 2000 CNOT gates and yet the data show no sign of a decaying signal. Note that the transients have died off after about 30 Trotter steps. In panel (b), the raw data with one to four resets is shown for up to 400 Trotter steps. After processing the data via extrapolating to the zero-reset-time limit and then correcting the result by shifting and stretching as described in the supplement 5, one can see that the post-processed data (c) agrees with the exact results to high precision. This simulation clearly shows the stability of driven-dissipative circuits on near-term quantum computers, producing accurate time evolution far longer than is currently possible with coherent dynamics of electrons[24].

Figure 2 shows the steady-state average DC current response of our system to an applied electric field calculated from elec-

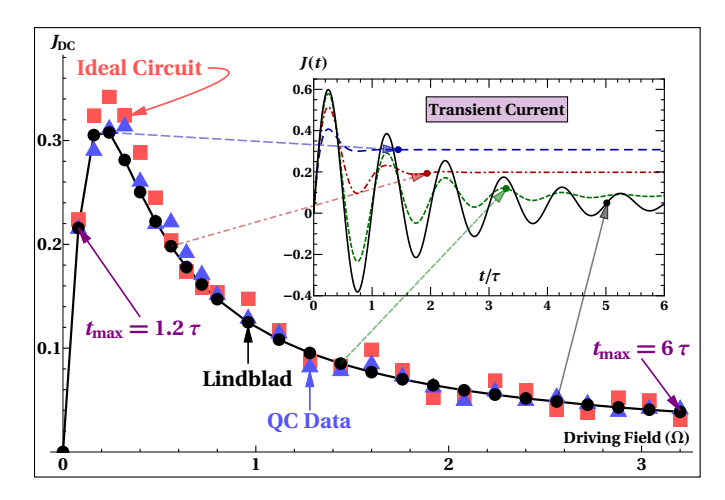


Figure 2: DC current versus electric field strength. Comparison of the DC response at a given field strength as computed (supplement 2) using: (i) the Lindblad master equation (black circles), (ii) the ideal circuit (red squares), and (iii) the measured data from <code>ibmq_boeblingen</code> (blue triangles). All circuits for the current were run for 50 Trotter steps each due to total quantum computer time available, leading to a trade-off between Trotter error and convergence error. Δt was chosen empirically such that $\Delta t/\tau$ is linear in Ω . Convergence to the steady-state current is shown in the inset with the solid dots representing $t_{\rm max}$ for that run.

tron density data as described in supplement 2. The data are post-processed in the same manner as in Fig. 1 and described in supplement 5, which is also compared against the ideal circuit and theoretical results from Lindblad techniques, as described in Ref. [28]. As shown in the inset of Fig. 2, the transient region extends to longer times as the electric field is increased, requiring the simulation to run further in time. Hence, the calculation requires a trade-off between Trotter error (large time step size) and convergence error (steady state not yet reached).

To minimize the total error, we choose Δt empirically with $\Delta t/\tau \approx 0.022 + 0.031\Omega$ (here, $\tau = 2\pi/\Omega$). At large driving fields it is clear that we have not yet reached the steady state and oscillations in the DC current data are observed even in the ideal case. At small driving field $\Delta t = \mathcal{O}(1/\Omega)$ and we incur large Trotter errors. Despite these limitations, the quantum computer results match the theoretical results fairly accurately across the entire range of simulated field strengths.

Atomic Limit

The second problem we simulate is the atomic limit of the driven-dissipative Hubbard model; in this limit, the electric

driving field drops out leaving just a dissipative problem. We take the Hubbard atom to be in an external magnetic field of magnitude B (in units of the Bohr magneton), with an on-site interaction of strength U and chemical potential μ . The Hamiltonian for this system reads

$$\mathcal{H} = U n_{\uparrow} n_{\downarrow} - \frac{\mu}{2} (n_{\uparrow} + n_{\downarrow}) - \frac{B}{2} (n_{\uparrow} - n_{\downarrow}) \tag{6}$$

where n_{α} is the occupation number operator for state $|\alpha\rangle$.

This is a strongly correlated electron problem, which can be simulated with four qubits. We build our dissipative circuit by using Kraus operators that induce transitions between computational basis states, which are the energy eigenstates. These transitions are implemented by mapping the system state to an ancilla register and rotating the system qubits controlled on the ancilla [29, 28] (shown in Fig. 3(a)); the approach uses just the transitions that correspond to a cycle through the states (depicted in Fig. 3(b)). Details are given in supplement 3. This circuit is iterated n times to simulate n Trotter steps of time evolution; here we use up to n = 19.

Figure 3 shows the transient evolution of the Hubbard atom from the vacuum state (with no electrons) to a thermal state with filling $n\approx 0.83$ at a temperature T=U/2 in an external magnetic field B=U/4 using one reset per Trotter step. These data are only post-processed for measurement-error corrections. The transient data lie close to the ideal circuit, but show deviations due to intrinsic errors in the hardware implementation. Nevertheless, the steady state is reproduced accurately for the four different populations of the thermal state (cf) and for the thermal density matrix (g-i). This further exemplifies the robustness of these types of algorithms to noise and how errors in early time steps are largely corrected in subsequent steps.

Conclusion

This work is a strong demonstration of the capabilities of near-term quantum hardware. It also leverages the newly developed capabilities of mid-circuit measurements and reset gates. These novel features are critical for building error-corrected, fault-tolerant quantum computers[30]; as we have shown, they are also essential for pushing the limits of NISQ computers. This convergence will drive further advances that can accelerate the development of fault-tolerant quantum computers. We anticipate for larger systems run on NISQ machines, there will be a robustness criterion that relates the fidelity of a single Trotter step to the level of dissipation in the system, implying that once one step is successful, then the map can be accurately continued to long times.

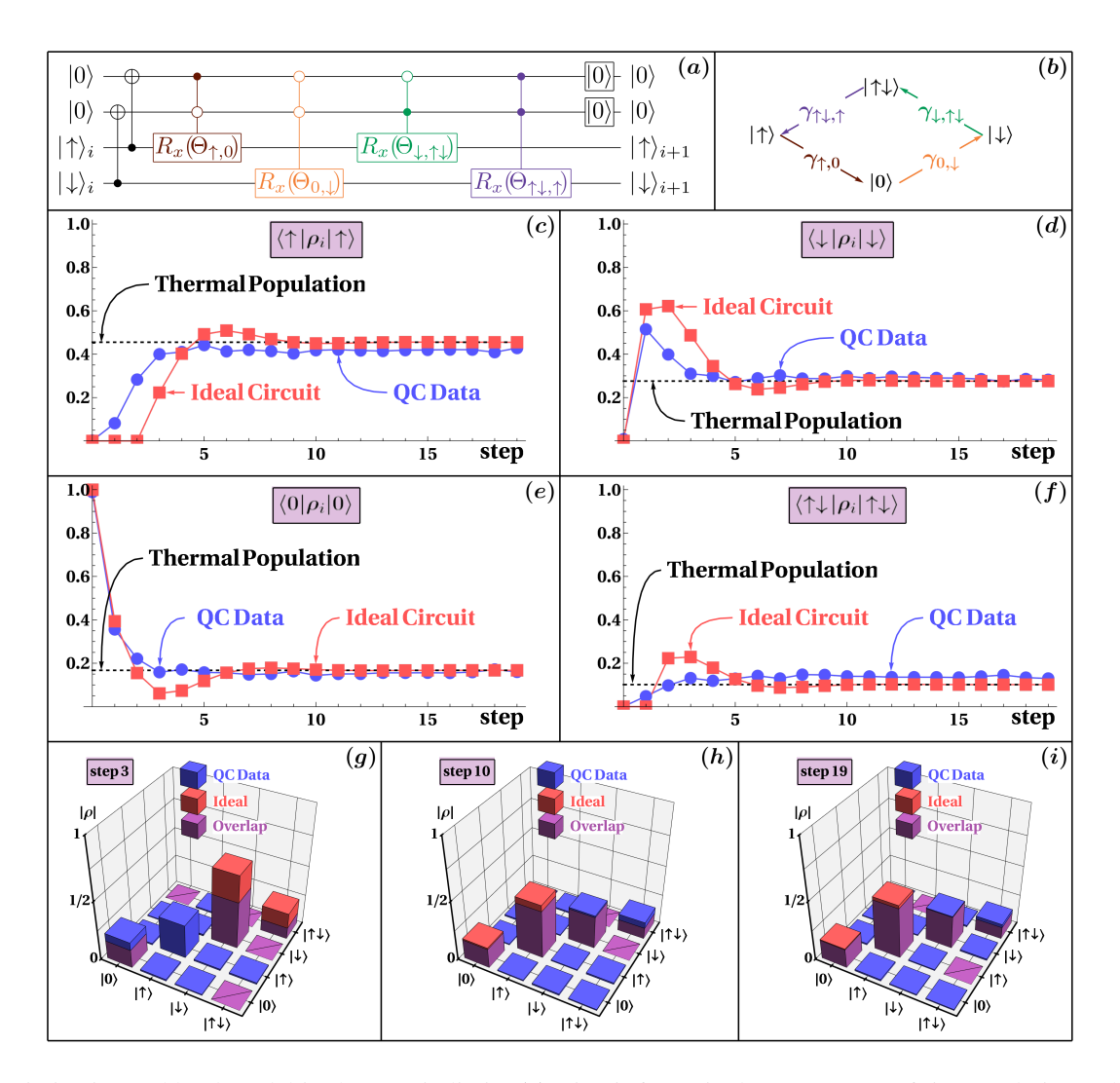


Figure 3: Dissipative Hubbard model in the atomic limit. (a) Circuit for a single Trotter step of time evolution. The rotation angles Θ are given in terms of transition probabilities γ , which are derived from the detailed balance condition as depicted in (b) and described in supplement 3. $\Theta_{i,j} = 2\sin^{-1}(\sqrt{\gamma_{i,j}})$ and $\gamma_{i,j} \propto e^{\beta\varepsilon_i}$, where ε_i is the energy of state $|i\rangle$. (c)–(f) Results showing the populations of each of the four possible occupation states versus Trotter step for the ideal case (red squares), measurement-error mitigated data from <code>ibmq_mumbai</code> (blue circles), and the theoretical thermal population (dashed black line). (g)–(i) Full tomography of the density matrix at selected time steps.

These successful demonstrations of two algorithmic primitives show that one can directly and robustly simulate the driven-dissipative Hubbard model on near-term quantum computers in both the non-interacting and atomic limits. This lays the groundwork to simulate the general driven-dissipative many-body problem on a quantum computer. Future research that builds on this foundation, aimed at properly combining these two algorithmic primitives to dissipate energy for arbitrary interactions, will solve the general problem and enable

quantum computers to simulate important real-world cases, such as pump-probe experiments, quark-gluon plasmas, and cavity-enhanced chemistry.

References

- [1] C. Giannetti, *et al.*, Ultrafast optical spectroscopy of strongly correlated materials and high-temperature superconductors: a non-equilibrium approach, *Adv. Phys.* **65**, 58 (2016).
- [2] E. Thyrhaug, *et al.*, Identification and characterization of diverse coherences in the fenna–matthews–olson complex, *Nature chemistry* **10**, 780 (2018).
- [3] M. Hertzog, M. Wang, J. Mony, K. Börjesson, Strong light-matter interactions: A new direction within chemistry, *Chem. Soc. Rev.* **48**, 937 (2019).
- [4] W. Cassing, E. Bratkovskaya, Parton-hadron-string dynamics: An off-shell transport approach for relativistic energies, *Nucl. Phys. A* **831**, 215 (2009).
- [5] H.-P. Breuer, F. Petruccione, *The theory of open quantum systems* (Oxford University Press on Demand, 2002).
- [6] O. E. Sommer, F. Piazza, D. J. Luitz, Many-body hierarchy of dissipative timescales in a quantum computer, *Phys. Rev. Research* **3**, 023190 (2021).
- [7] B. Rost, *et al.*, Simulation of thermal relaxation in spin chemistry systems on a quantum computer using inherent qubit decoherence, *arXiv preprint arXiv:2001.00794* (2020).
- [8] C. Tseng, et al., Quantum simulation with natural decoherence, *Phys. Rev. A* **62**, 032309 (2000).
- [9] B. M. Terhal, D. P. DiVincenzo, Problem of equilibration and the computation of correlation functions on a quantum computer, *Phys. Rev. A* **61**, 022301 (2000).
- [10] H. Wang, S. Ashhab, F. Nori, Quantum algorithm for simulating the dynamics of an open quantum system, *Phys. Rev. A* **83**, 062317 (2011).
- [11] H.-Y. Su, Y. Li, Quantum algorithm for the simulation of open-system dynamics and thermalization, *Phys. Rev. A* **101**, 012328 (2020).
- [12] Z. Hu, R. Xia, S. Kais, A quantum algorithm for evolving open quantum dynamics on quantum computing devices, *Scientific reports* **10**, 1 (2020).
- [13] Z. Hu, K. Head-Marsden, D. A. Mazziotti, P. Narang, S. Kais, A general quantum algorithm for open quantum dynamics demonstrated with the fenna-matthews-olson complex, *arXiv* preprint arXiv:2101.05287 (2021).

- [14] K. Head-Marsden, S. Krastanov, D. A. Mazziotti, P. Narang, Capturing non-markovian dynamics on nearterm quantum computers, *Phys. Rev. Research* 3, 013182 (2021).
- [15] A. M. Childs, T. Li, Efficient simulation of sparse Markovian quantum dynamics, *Quantum Information and Computation* **17**, 901 (2017).
- [16] M. Kliesch, T. Barthel, C. Gogolin, M. Kastoryano, J. Eisert, Dissipative quantum church-turing theorem, *Phys. Rev. Lett.* **107**, 120501 (2011).
- [17] T. Haug, K. Bharti, Generalized quantum assisted simulator, *arXiv preprint arXiv:2011.14737* (2020).
- [18] N. Yoshioka, Y. O. Nakagawa, K. Mitarai, K. Fujii, Variational quantum algorithm for nonequilibrium steady states, *Phys. Rev. Research* **2**, 043289 (2020).
- [19] H. Kamakari, S.-N. Sun, M. Motta, A. J. Minnich, Digital quantum simulation of open quantum systems using quantum imaginary time evolution, *arXiv preprint arXiv:2104.07823* (2021).
- [20] M. Metcalf, J. E. Moussa, W. A. de Jong, M. Sarovar, Engineered thermalization and cooling of quantum manybody systems, *Phys. Rev. Research* **2**, 023214 (2020).
- [21] J. T. Barreiro, *et al.*, An open-system quantum simulator with trapped ions, *Nature* **470**, 486–491 (2011).
- [22] S. Tornow, W. Gehrke, U. Helmbrecht, Non-equilibrium dynamics of a dissipative two-site hubbard model simulated on the ibm quantum computer, *arXiv* preprint *arXiv*:2011.11059 (2020).
- [23] J. Preskill, *Introduction to quantum computation and information* (World Scientific, 1998), pp. 213–269.
- [24] F. Arute, *et al.*, Observation of separated dynamics of charge and spin in the fermi-hubbard model, *arXiv* preprint arXiv:2010.07965 (2020).
- [25] P. Zanardi, L. C. Venuti, Geometry, robustness, and emerging unitarity in dissipation-projected dynamics, *Phys. Rev. A* **91**, 052324 (2015).
- [26] S. Schirmer, X. Wang, Stabilizing open quantum systems by markovian reservoir engineering, *Phys. Rev. A* 81, 062306 (2010).

- [27] D. Jaschke, L. D. Carr, I. de Vega, Thermalization in the quantum ising model—approximations, limits, and beyond, *Quantum Science and Technology* **4**, 034002 (2019).
- [28] L. Del Re, B. Rost, A. Kemper, J. Freericks, Drivendissipative quantum mechanics on a lattice: Simulating a fermionic reservoir on a quantum computer, *Phys. Rev. B* **102**, 125112 (2020).
- [29] J. T. Barreiro, *et al.*, An open-system quantum simulator with trapped ions, *Nature* **470**, 486 (2011).
- [30] D. A. Lidar, T. A. Brun, *Quantum error correction* (Cambridge university press, 2013).
- [31] H. Abraham, *et al.*, Qiskit: An open-source framework for quantum computing (2019).
- [32] A. Kandala, *et al.*, Error mitigation extends the computational reach of a noisy quantum processor, *Nature* **567**, 491 (2019).

Acknowledgements

We acknowledge use of the IBM Quantum devices and the IBM Quantum Hub at North Carolina (NC) State for this paper.

Funding:

US Department of Energy, Office of Science, Basic Energy Sciences, Division of Materials Sciences and Engineering under Grant No. DE-SC0019469 (JKF, AFK, LDR, BR)

McDevitt bequest at Georgetown (JKF)

National Science Foundation QISE-NET Award No. DMR-1747426 (BR)

Aspen Center for Physics through National Science Foundation Grant No. PHY-1607611 (BJ)

Author contributions:

Conceptualization: AFK, BR, JKF, LDR

Formal analysis: BR, LDR

Funding acquisition: AFK, BJ, JKF

Resources: AFK, BJ, BR Investigation: BR, LDR, NE Methodology: BR, LDR, NE

Visualization: BR

Project administration: AFK, BJ, and JKF Writing – original draft: BR, JKF, LDR, NE

Writing - review & editing: AFK, BJ, BR, JKF, LDR, NE

Supplementary Materials

1 Materials and Methods

All data were taken using quantum computers made available by IBM, either ibmq_mumbai (Fig. 1(a) and Fig. 3) or ibmq_boeblingen (Fig. 1(b,c) and Fig. 2). ibmq_boeblingen is a 20-qubit quantum device and ibmq_mumbai is 27-qubit device. The reported error rates were used to select sets (~5-10) of candidate qubits on which a limited number of Trotter steps were run. Results from these were then used to select the final qubits on which the full job(s) would be run. Raw shot counts were processed using Qiskit Ignis'[31] built in measurement error mitigation protocol. This prepares and immediately measures each computational basis state giving a confusion matrix, which is inverted and applied to the raw shot counts to yield the mitigated shot counts.

This work pushed current near-term quantum computers to their limits. This created some unique issues when trying to run these extremely deep circuits. We encountered buffer overflow errors after running a large number of our larger circuits indicating we had overflowed the device's capacity to record more measurement data. This is why we limited our DC current data to 50 Trotter steps per unique set of parameter values. We avoided this limit when taking data for Fig. 1(b) by breaking our jobs into smaller chunks, but this meant long queue times, which would have been prohibitive to get the data in Fig. 2. The data in Fig. 1(a) were obtained through exclusive access to ibmq_mumbai, which allowed us to break our circuits into individual jobs without worrying about queue times. Nevertheless, we still overflowed the buffer around step 300, forcing us to change to a new pair of qubits with a fresh buffer. Finally, we began to exceed the limits of the system generating the driving microwave pulses at around 1000 Trotter steps, which is why this is the upper limit for Fig. 1(a).

For the full tomography results in Fig. 3, we made use of the "state tomography circuits" and "StateTomographyFitter" functions built into Qiskit Ignis. The "state tomography circuits" creates a list of 3^n circuits which carries out the desired quantum circuit and then measures in the X, Y, and Z bases. These results are then fed into the "StateTomographyFitter.fit" function in order to reconstruct the full quantum state.

2 Lattice electrons driven by a DC field

The open quantum system examined in the first part of the paper is given by non-interacting fermions on a one-dimensional lattice with nearest-neighbor hopping and driven out of equilibrium by an electric field. The effect of the field is taken into account by introducing a complex Peierls phase $\varphi(t) = \Omega t$ (given by $\Omega = eEa$) to the hopping amplitude γ_h . The system Hamiltonian then reads:

$$\hat{\mathcal{H}} = -\gamma_h \sum_{i} e^{i\varphi(t)} d_i^{\dagger} d_{i+1} + \text{h. c.}$$
(S.1)

We let the system interact with a thermostat by coupling every lattice site to an independent fermionic reservoir, whose Hamiltonian is $\hat{\mathcal{H}}_b = \sum_{i\alpha} \omega_\alpha c_{i\alpha}^\dagger c_{i\alpha}$, through a hopping term that is given by:

$$\hat{\mathcal{V}} = -g \sum_{i\alpha} \left(d_i^{\dagger} c_{i\alpha} + c_{i\alpha}^{\dagger} d_i \right). \tag{S.2}$$

Here g is the bare hybridization amplitude, and α is an index that runs over all the internal degrees of freedom of the reservoir, which are taken to be infinite. The total Hamiltonian of the system plus the reservoir is given by $\hat{\mathcal{H}}_{tot} = \hat{\mathcal{H}} + \hat{\mathcal{H}}_b + \hat{\mathcal{V}}$ and can be block diagonalized by expanding the fields in their Fourier components; that is, $d_k = \frac{1}{\sqrt{N}} \sum_n d_n e^{-ikn}$, $c_{k\alpha} = \frac{1}{\sqrt{N}} \sum_n c_{n\alpha} e^{-ikn}$. In this basis, the Hamiltonian decomposes into a sum of Hamiltonians for each momenta, $\hat{\mathcal{H}}_{tot} = \sum_k \hat{\mathcal{H}}_{tot}^{(k)}$, with $\hat{\mathcal{H}}_{tot}^{(k)} = \hat{\mathcal{H}}_b^{(k)} + \hat{\mathcal{H}}_b^{(k)} + \hat{\mathcal{V}}_b^{(k)}$ and where

$$\hat{\mathcal{H}}^{(k)}(t) = -2\gamma_h \cos(k + \Omega t) d_k^{\dagger} d_k, \tag{S.3}$$

$$\hat{\mathcal{H}}_b^{(k)} = \sum_{\alpha} \omega_{\alpha} c_{k\alpha}^{\dagger} c_{k\alpha}, \tag{S.4}$$

$$\hat{\mathcal{V}}^{(k)} = -g \sum_{\alpha} d_k^{\dagger} c_{k\alpha} + \text{h. c.}$$
(S.5)

The Lindblad master equation of the density matrix for a given k-point then becomes

$$\partial_t \rho_k = -i[\mathcal{H}_k(t), \rho_k] + \sum_{\ell = \{1, 2\}} L_\ell \, \rho_k \, L_\ell^{\dagger} - \{\rho_k, L_\ell^{\dagger} L_\ell\}, \tag{S.6}$$

where the Lindblad operators are $L_1 = \sqrt{\Gamma n_F(\epsilon_k(t))} d_k$ and $L_2 = \sqrt{\Gamma n_F(-\epsilon_k(t))} d_k^{\dagger}$, with $\Gamma = g^2 N(0)$ and N(0) being the reservoir DOS evaluated at the Fermi level (see Ref.[28] for further details on the formal derivation).

The driven electric current is found from

$$J = \frac{\gamma_h}{\pi} \int dk \sin(k + \Omega t) n_k(t), \tag{S.7}$$

where $n_k(t) = \text{Tr}\left[\rho_k(t)d_k^{\dagger}d_k\right]$. By multiplying Eq. S.6 times $d_k^{\dagger}d_k$ and computing the trace of both sides of the equation, we obtain the following differential equation for the momentum distribution function $\dot{n}_k = -2\Gamma(n_k(t) - n_F(\epsilon_k(t)))$. Solving yields

$$n_k(t) = n_k(0)e^{-2\Gamma t} + 2\Gamma \int_0^t ds \, e^{-2\Gamma(t-s)} n_F[\epsilon(k+\Omega s)].$$
 (S.8)

Next introduce the gauge-invariant wave vector $k_m = k + \Omega t$ into the integral

$$n_k(t) = n_k(0)e^{-2\Gamma t} + 2\Gamma \int_0^t ds \, e^{-2\Gamma(t-s)} n_F[\epsilon(k_m + \Omega(s-t))].$$
 (S.9)

Then for $t \to \infty$ at fixed k_m , we can perform the change of coordinates $y = k_m + \Omega(s-t)$ to yield the following formula for the momentum distribution function:

$$n(k_m) = \frac{2\Gamma}{\Omega} \int_{-\infty}^{k_m} dy \, e^{\frac{2\Gamma}{\Omega}(y - k_m)} n_F[\epsilon(y)], \tag{S.10}$$

which depends only on k_m . This implies that for large enough time, we can reconstruct the full momentum distribution function by fixing the value of the crystalline momentum k and letting t run over one full Floquet period. In practice, we use the fact that the transients die off quickly to use the data averaged over one Floquet period to represent the long-time limit of the momentum distribution.

3 Atomic Hubbard circuit

We describe how to dissipatively prepare the thermal state of the atomic limit of the Hubbard model on a pair of qubits. Our Hamiltonian is given by

$$\mathcal{H} = U n_{\uparrow} n_{\downarrow} - \frac{\mu}{2} (n_{\uparrow} + n_{\downarrow}) - \frac{B}{2} (n_{\uparrow} - n_{\downarrow}) \tag{S.11}$$

where U is the on-site interaction strength, μ is the chemical potential, B is the magnetic field in units of the Bohr magneton, and n_{α} is the occupation number operator for state $|\alpha\rangle$. Our desired mixed state is then $\tilde{\rho}=e^{-\beta\mathcal{H}}/\operatorname{Tr}e^{-\beta\mathcal{H}}$ where β is the inverse temperature of the thermal state.

We prepare this state by iteratively applying a dissipative map, \mathcal{E} , to the qubits such that $\tilde{\rho}$ is the unique fixed point of \mathcal{E} . We define \mathcal{E} by a set of Kraus operators $\{K_i\}$ such that

$$\rho_{i+1} = \mathcal{E}(\rho_i) = \sum_s K_s \rho_i K_s^{\dagger} \quad \text{with} \quad \sum_s K_s^{\dagger} K_s = 1 \quad \text{and} \quad \mathcal{E}(\tilde{\rho}) = \tilde{\rho}. \tag{S.12}$$

Such a map may be realized by choosing Kraus operators which induce transitions between eigenstates of the Hamiltonian $(|j\rangle\langle i|)$ with fixed transition probabilities $(\gamma_{i,j})$. These transition probabilities define a detailed-balanced condition,

$$\sum_{j} \gamma_{i,j} \langle i | \rho | i \rangle = \sum_{j} \gamma_{i,j} \langle j | \rho | j \rangle, \tag{S.13}$$

i.e. the density transitioning out of each state is exactly balanced by the density transitioning in. When this condition is met, ρ is a fixed point of \mathcal{E} . To reduce the complexity of the final circuit, we take only a minimal set of these transitions that correspond to a cycle through the states as depicted in Fig. 3(b).

Solving Eq. S.13 reveals $\gamma_{i,j}$ is proportional to the inverse Boltzmann factor for state i, i.e. $\gamma_{i,j} = \mathcal{N} \ e^{\beta \varepsilon_i}$ where ε_i is the energy of state $|i\rangle$ given by $\mathcal{H} |i\rangle = \varepsilon_i \, |i\rangle$. \mathcal{N} can be thought of as an effective time step or system/reservoir coupling strength. Because \mathcal{E} must satisfy the normalization condition given in Eq. S.12, we find $0 \le \gamma_{i,j} \le 1$ which bounds the values \mathcal{N} can take. To maximize convergence speed, we take \mathcal{N} to be such that the largest $\gamma_{i,j}$ is 1.

Armed with the Kraus operators, we can build a circuit that implements $\mathcal E$ in a straightforward way. Note that the eigenstates of $\mathcal H$ are the computational-basis states, so we can transition between states with single-qubit rotations. To do this, we first map the state of the system onto an ancilla register. Then we rotate the system qubits, controlled on the ancilla register, to implement the transitions. A transition probability of $\gamma_{i,j}$ is achieved with rotation angle $\theta_{i,j}=2\sin^{-1}(\sqrt{\gamma_{i,j}})$. Finally the ancilla qubits are reset in preparation for the next step. This circuit is shown in Fig. 3(a) and yields Kraus operators of the form $K_{i,j}=\sqrt{1-\gamma_{i,j}}\,|i\rangle\langle i|-i\sqrt{\gamma_{i,j}}\,|j\rangle\langle i|$, as desired.

Ultimately this circuit needs to be transpiled down into IBM's native gates and conform to the qubit connectivity in a real device. This was done in part by hand and in part using the transpilation tools in Qiskit, the result of which is shown in Fig. S1.

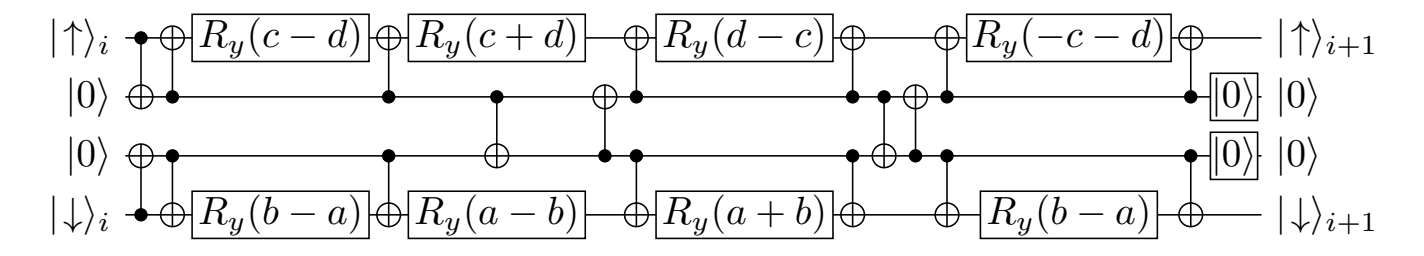


Figure S1: The circuit from Fig. 3(a) transpiled into CNOT gates and single-qubit rotations suitable for nearest neighbor connectivity. We have adopted the shorthand $a = \Theta_{\uparrow\downarrow,\uparrow}/2$, $b = \Theta_{0,\downarrow}/2$, $c = \Theta_{\downarrow,\uparrow\downarrow}/2$, $d = \Theta_{\uparrow,0}/2$. We note that this circuit is the same as that shown in Fig. 3(a) up to a unitary on the ancilla register before resetting and an $R_z(\pm\pi/2)$ gate before the first Trotter step and after the last Trotter step on both system qubits. These differences leave the dissipative map $\mathcal E$ unaffected with the initial $R_z(\pi/2)$ being absorbed into the initial state.

4 Error model

The ideal curve for the steady state of the electron density, $n_k(t)$, is distorted by errors occurring in the quantum computer during the run. We can model this new distorted curve well by taking into account only two sources of error: 1) imperfect reset gates and 2) the T_1 decay of the system qubit.

We first discuss the reset gates. In IBM's hardware, a reset gate is performed by measuring the state of a qubit and then applying an X gate if the qubit was measured to be in the $|1\rangle$ state and leaving it in the $|0\rangle$ state otherwise. However, even

assuming a perfect X gate, measurement fidelity is imperfect and so we expect an imperfect reset gate. Call the probability of measuring m, given the qubit is actually in $|m\rangle$ to be $p(m|m) \equiv p_m$. If the qubit is initially in state ρ with $\langle 0|\rho|0\rangle = a_0$, then we model the state of the qubit after one reset gate, ρ_1 , to be characterized by

$$\langle 0|\rho_1|0\rangle = a_0(p_0 - p_1) + p_1 \quad \text{and} \quad \langle 0|\rho_1|1\rangle = 0.$$
 (S.14)

In IBM's hardware, we have $p_0 \ge p_1$, so we can improve the fidelity of a reset operation by applying multiple reset gates in succession. Call the qubit state after r reset gates ρ_r . Given the above model, we expect the probability of a successful reset to be

$$\langle 0|\rho_r|0\rangle = a_0 \left(p_0 - p_1\right)^r + \frac{p_1 \left(1 - \left(p_0 - p_1\right)^r\right)}{1 - p_0 + p_1}.$$
(S.15)

This simple model of reset infidelity appears sufficient to explain most of the observed results. We find $p_0 = 0.97$ and $p_1 = 0.91$ on average over all our runs.

Now, we discuss the T_1 decay. Because a reset gate is approximately an order of magnitude longer than the combined duration of the other operations in a single Trotter step, we assume all of amplitude damping of the system qubit occurs during the time it takes for the reset operation on the ancilla qubit. We can model the amplitude damping channel as performing the following map on a single qubit: $\rho \mapsto \sum_k M_k \rho M_k^{\dagger} \equiv \mathcal{E}_x(\rho)$ where $M_k \in \left\{ \sqrt{1-e^{-rT}}|0\rangle\langle 1| \; , \; |0\rangle\langle 0| + \sqrt{e^{-rT}}|1\rangle\langle 1| \right\}$ are the Kraus operators for the amplitude damping channel, T is the duration of a single reset gate in units of the T_1 time of the system qubit, and r is the number of reset gates used in a reset operation. We find the average duration of a reset gate is approximately 6% of the system qubit T_1 time.

Putting these together with the circuit shown in Fig. 1(d) gives our error model. Call ρ_s^S and ρ_s^a the density matrix of the system and ancilla at Trotter step s (or time $t=s\Delta t$), respectively. Because the error incurred during a single Trotter step propagates non-trivially to the next steps, we express our model below in terms of recursive formulae for the populations $n_s \equiv \langle 0 | \rho_s^S | 0 \rangle$ and $a_s \equiv \langle 0 | \rho_s^a | 0 \rangle$. We explicitly represent the unitary part of the circuit for step s as a matrix s so that applying the circuit to a generic two-qubit state s0 gives s1. This yields

$$\rho_{s+1} = \rho_{s+1}^a \otimes \mathcal{E}_x \left(\text{Tr}_a \left[U_s (\rho_s^a \otimes \rho_s^S) U_s^{\dagger} \right] \right), \tag{S.16}$$

which leads to the following coupled recurrence relations

$$n_{s+1} = 1 - e^{-rT} \left((2a_s - 1) \left(2\Gamma \Delta t \left(n_s - n_F[\varepsilon_s] \right) - n_s \right) + a_s \right)$$
 (S.17)

$$a_{s+1} = \frac{a_s + 2\Gamma\Delta t \left(2a_s - 1\right) \left(\left(n_s - 1\right) n_F[\varepsilon_s] - n_s n_F[-\varepsilon_s]\right)}{\left(p_0 - p_1\right)^{-r}} + \frac{p_1 \left(1 - \left(p_0 - p_1\right)^r\right)}{1 - p_0 + p_1}.$$
 (S.18)

Here $\varepsilon_s \equiv -2\cos(k+\Omega s\Delta t)$ is the dispersion relation, $n_F[x]$ is the Fermi-Dirac distribution, and the angles at step s are defined by

$$\theta_s = 2\sin^{-1}\sqrt{\frac{2\Gamma\Delta t}{e^{\beta\varepsilon_s} + 1}}$$
 and $\phi_s = 2\sin^{-1}\sqrt{\frac{2\Gamma\Delta t}{e^{-\beta\varepsilon_s} + 1}}$ (S.19)

These recurrence relations can easily be solved numerically. We use an optimizer to find $T=0.06T_1$, $p_0=0.97$, and $p_1=0.91$, which best match our data. The same values for T, p_0 , and p_1 are used for each r=1,2,3, and 4 iterated reset gates per reset operation, since the parameters should be approximately constant for a given pair of qubits on a given quantum device. A comparison of the error model vs. ideal circuit vs. actual quantum computer data is shown in Fig. S2.

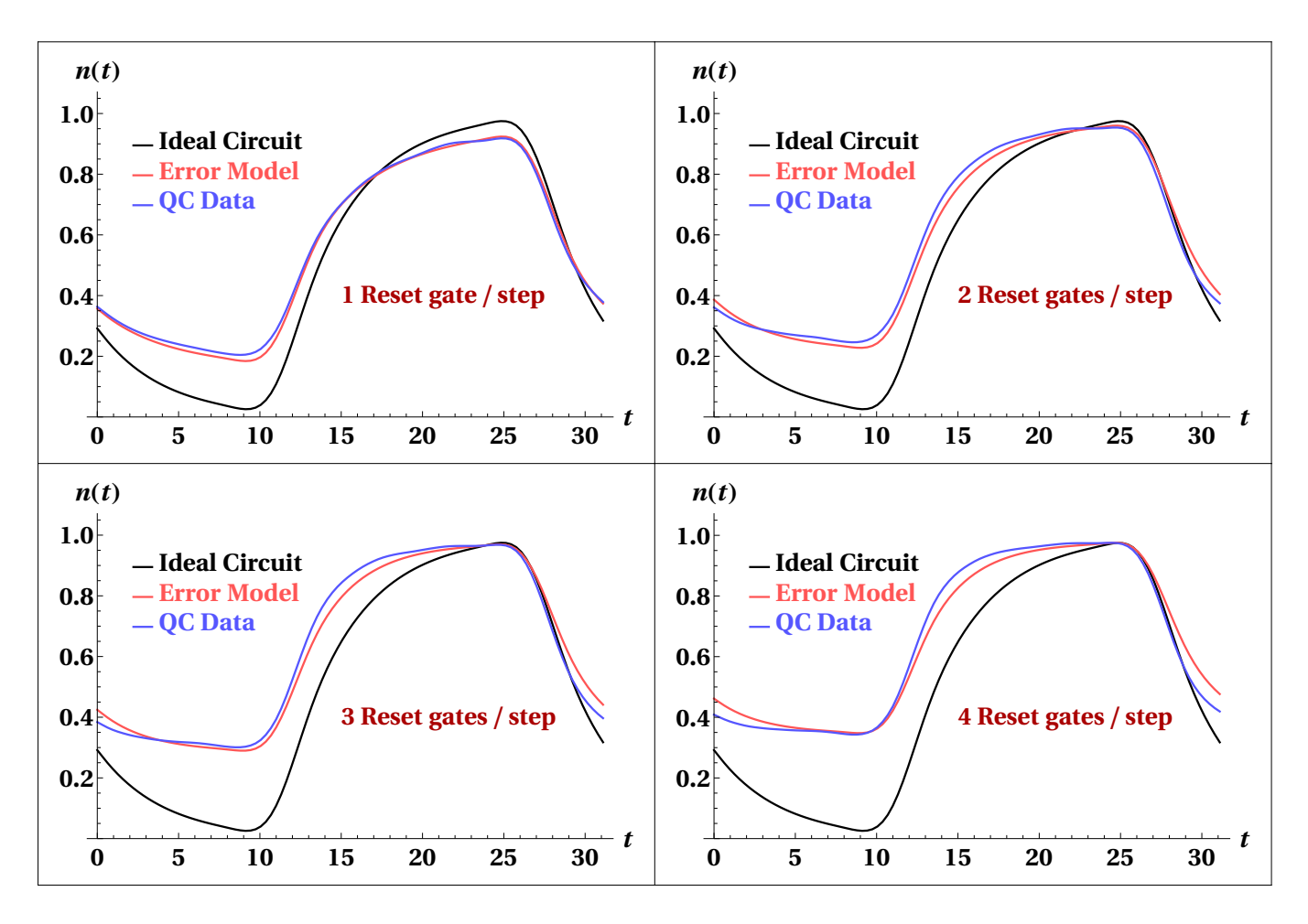


Figure S2: Comparison of the ideal circuit, our error model and the actual data from the quantum computer for r = 1, 2, 3, and 4 reset gates per Trotter step. The ideal circuit and quantum computer data are the same as shown in Fig. 1. The error model and data agree well overall and adequately explain the majority of the error observed.

This error model also gives insight into why our system, and dissipative systems in general, are robust against noise. Inspecting Eq. S.17 shows that n_{s+1} (the electron density at step s+1) depends on n_s as $e^{-rT}(2a_s-1)(2\Gamma\Delta t-1)n_s$. Furthermore, we have $0 \le e^{-rT}$, $2a_s-1 \le 1$, and $0 \le 2\Gamma\Delta t-1 < 1$ when $\Gamma > 0$, i.e. when dissipation is non-zero. This tells us that the effect of an error at step s on the density at step s' > s is exponentially small in s' - s. This further suggests that if we have a sufficiently small base error rate, the compounding effect of these errors are offset by the dissipation, and this is why our error model does not need to take into account other errors, such as gate errors.

We can get an intuitive sense for how this works if we make the assumption that $a_s = a_0$ for all s, i.e. reset fidelity is independent of the qubit state. This is a good assumption when $p_0 \approx p_1$ or $r \gg 1$ since the reset fidelity depends on the qubit state through $\langle 0 | \rho_a | 0 \rangle (p_0 - p_1)^r$. This then recasts Eq. S.17 as

$$n_{s+1} = 1 - e^{-rT} \left((2a_0 - 1) \left(2\Gamma \Delta t \left(n_s - n_F[\varepsilon_s] \right) - n_s \right) + a_0 \right)$$
 (S.20)

for which Mathematica gives the analytic solution of the recurrence relation for n_s , $s \gg 1$ as

$$\frac{1}{2} + \frac{1 - e^{-rT}}{2(1 - a_0 e^{-rT}(1 - 2\Gamma\Delta t))} - \frac{a_0}{e^{rT}} \Gamma \Delta t \sum_{t=0}^{s-1} \tanh\left(\frac{\beta \varepsilon_t}{2}\right) \left(\frac{a_0}{e^{rT}}(1 - 2\Gamma\Delta t)\right)^{s-t-1}.$$
 (S.21)

Plugging in $a_0 = 1$ and T = 0 recovers the error free solution

$$\frac{1}{2} - \Gamma \Delta t \sum_{t=0}^{s-1} \tanh\left(\frac{\beta \varepsilon_t}{2}\right) \left((1 - 2\Gamma \Delta t) \right)^{s-t-1}. \tag{S.22}$$

These two solutions are qualitatively the same. They differ by a shift (second term in Eq S.21), a stretch of a_0e^{-rT} and deformation in shape equivalent to using Γ' instead of Γ , such that $(1-2\Gamma'\Delta t)=a_0e^{-rT}(1-2\Gamma\Delta t)$. This shows that the errors in the quantum hardware tend to perturb but not destroy the steady-state dynamics. We anticipate this result to hold true for many dissipative algorithms—as we can consider the error channels occurring inside the quantum computer to supplement the dissipative channels we are explicitly simulating. As long as the error rates are low and/or our dissipation rate is high, we should expect to reach a nearly error-free steady state.

5 Processing $n_k(t)$

After the transients have died (about 30 Trotter steps for the data in Fig. 1), the population of the $|0\rangle$ state gives our raw data for $n_k(s\Delta t)$. We then correct this data for measurement errors using the built in tools in Qiskit Ignis[31] to obtain the steady state data (e.g. data with green background in Fig. 1(b)). We then discard these first Trotter steps as transient data. The remaining data is (ideally) periodic according to Floquet theory with a period of $\tau=2\pi/\Omega$, since our Hamiltonian is periodic with the same period (even though the field is DC, it drives periodic Bloch oscillations, making the system periodic). Because the step size Δt is not always commensurate with the Floquet period, we use quadratic interpolation to generate a smooth curve, on a common time grid, and average together distinct periods to obtain an averaged curve for $n_k^{\rm ave}(t)$ over a single period

$$n_k^{\text{ave}}(t) = \sum_{\ell=0}^{(t_{\text{max}}-t)/\tau} n_k(t+\ell\tau),$$
 (S.23)

where t lies on the common time grid. It is from this quantity that steady-state observables (e.g. DC current) can be calculated.

The constructed $n_k^{\text{ave}}(t)$ is distorted by errors occurring within the quantum computer, as detailed in supplement 4. However, we can correct for the majority of this distortion. First, we know that $\int_0^\tau dt n_k(t) = 0.5$, which allows us to center the momentum distribution curve about its true midpoint (at $n_k = 0.5$). Second, we ran our circuits with r = 1, 2, 3, and 4 native reset gates per Trotter step. We would like to be able to scale our results to an instantaneous application time for the resets, similar to Richardson extrapolation[32]. But, while the additional reset gates do boost the fidelity of the reset operation, they also add decoherence errors, because the gates are non-negligibly long compared to the T_1 time of the qubits, as described in supplement 4. For this work, we find a negligible difference in reset fidelity between r = 2, 3, 4. This then allows us to extrapolate to r = 0, the limit of no T_1 decay.

As can be seen in supplement 4, the functional dependence of $n_k(t)$ on T_1 errors is complex and so we opt for using a simple quadratic extrapolation. Doing this tends to be reasonably effective in improving the data. However, this does nothing to correct reset infidelity. Furthermore, when we have a limited number of periods of steady-state data, or when Ω is large and the curves are quite flat, noise from counting statistics and other random errors inside the quantum computer make the extrapolation less reliable. This is especially true when computing the DC response, which is quite sensitive to the shape of $n_k(t)$. To mitigate these issues, we correct the amplitude by computing the theoretical maximum of $n_k(t)$ at zero temperature and then use that as an approximate scale factor. Starting with our master equation in terms of our gauge-invariant wavevector, $k_m = k + \Omega t$, we have

$$\dot{n}(k_m) = 2\Gamma\left(\frac{1}{1 + e^{2\beta\cos k_m}} - n(k_m)\right). \tag{S.24}$$

Taking the zero temperature limit, $\beta \to \infty$, gives

$$\dot{n}(k_m) = \Gamma \left(1 + \text{sgn} \left(\cos k_m \right) - n(k_m) \right) \to \begin{cases} \cos k_m < 0 & \dot{n} = -2\Gamma n \\ \cos k_m > 0 & \dot{n} = 2\Gamma (1 - n). \end{cases}$$
(S.25)

Since $0 \le n \le 1$, the derivative changes sign when $\cos k_m = 0$. But the solution for $n(k_m)$ actually ranges from a minimal value larger than 0 to a maximal value smaller than 1. The differential equation can be immediately solved, and we find that

$$n_{\text{max}} = \frac{1}{2} \left(1 + \tanh \frac{\pi \Gamma}{\Omega} \right). \tag{S.26}$$

We use this value to stretch the curves about 1/2 (their midpoint), which gives our final curve. Despite the distortions remaining after the extrapolation due to reset infidelity, uncorrected T_1 effects and other sources of error, we generally find excellent agreement between the ideal result and our final post-processed curve.